Towards a relationship between photoluminescence emissions and photocatalytic activity of Ag_2SeO_4: Combining experimental data and theoretical insights

Ivo M. Pinatti [a,b*], Ana C. M. Tello [c,d], Paula F. S. Pereira [c], Aline B. Trench [c], Marcio D. Teodoro [e], Ieda L. V. Rosa [c], Albérico B. F. da Silva [d], Elson Longo [c], Juan Andrés [b*], and Alexandre Z. Simões [a]

[a] *Faculty of Engineering of Guaratinguetá, São Paulo State University (UNESP), 12516-410, Guaratinguetá, SP, Brazil.*
[b] *Department of Analytical and Physical Chemistry, University Jaume I (UJI), Castelló 12071, Spain.*
[c] *CDMF, LIEC, Federal University of São Carlos (UFSCar), P.O. Box 676, São Carlos 13565-590, Brazil.*
[d] *São Carlos Institute of Chemistry, São Paulo University (USP), P.O. Box 676, São Carlos 13566-905, Brazil.*
[e] *Physics Department, Federal University of São Carlos (UFSCar), P.O. Box 676, São Carlos 13565-905, Brazil.*

**corresponding authors: ivo.m.pinatti@unesp.br; andres@qfa.uji.es*

Abstract

A systematic theoretical and experimental study was carried out to find a relationship between photoluminescence emissions and photocatalytic activity of Ag_2SeO_4 obtained by different synthesis methods (sonochemistry, ultrasonic probe, coprecipitation and microwave assisted hydrothermal synthesis). Experimental characterization techniques (XRD with Rietveld refinement, Raman, FTIR, UV-vis, XPS and photoluminescence spectroscopies) were performed to elucidate its structural order at short, medium, and long ranges. Morphological analysis evaluated by FE-SEM showed distinct morphologies due to the different methods of synthesis. Based on density functional theory (DFT) calculations it was possible to study in detail the Ag_2SeO_4 surface properties, including its surface energy, geometry, and electronic structure for the (100), (010), (001), (101), (011), (110), (111), (021), (012) and (121) surfaces. The equilibrium morphology of Ag_2SeO_4 was predicted as a truncated octahedron with exposed (111), (001), (010) and (011) surfaces. Photoluminescence emissions showed a band covering the visible spectrum, and the Ag_2SeO_4 obtained by the coprecipitation method presented the most intense band with a maximum in the red region. Photocatalytic results confirmed that Ag_2SeO_4 synthesized by sonochemistry method is the best photocatalyst for Rhodamine B degradation under UV light irradiation.

Introduction

In the scientific community, the family of selenium-based materials stands out due to the existence of a great variety of compounds. They act as outstanding materials because of the various oxidation states that selenium can acquire, thus resulting in different structures. [1–20] Divalent metallic selenates and selenites with the general formulas $MSeO_4$ and $MSeO_3$ (M = Mg, Ca, Sr, Ba, Cd, Pb, Sn, Mn, Co, Ni, Cu, Zn), respectively, have been considered promising due to their excellent good performance in many applications in different areas. [21–26] On the contrary, monovalent metallic selenates and selenites are still scarce. Particularly, silver selenate (Ag_2SeO_4) presents an orthorhombic crystal system and space group *Fddd* at room temperature. Together with its lattice energies and associated thermodynamic properties [27], its polymorphism and phase diagram at high pressures and temperatures were ~~also~~ calculated. [28–31] Concerning its applications, the performance of button-type lithium cells based on Ag_2SeO_4 as cathode in various organic electrolytes was evaluated. [32] In addition, the growth of single crystals of Ag_2SeO_4 in silica gels [33] and its correspondent Ni^{2+}/Cu^{2+} doping was investigated. [34] Lastly, some works reported the structure, characterization, and physicochemical properties of superionic conducting glasses of the system based on Ag_2SeO_4 [35–39] among others [40–43].

Recently, our group obtained Ag_2SeO_3 by different synthesis methods, besides elucidating its structural, electronic, optical, and photocatalytic properties [44]. As a continuation of this research line, in this work we report the synthesis of Ag_2SeO_4 by sonochemistry (SC), ultrasonic probe (UP) coprecipitation (CP), and microwave-assisted hydrothermal (MH) methods. XRD, Rietveld refinement, Raman, FTIR, UV-vis, XPS and photoluminescence spectroscopies were used to characterize the microcrystals. In addition, first-principles calculations within the framework of the density functional theory (DFT) were employed to obtain atomic-level information of the bulk and surfaces of Ag_2SeO_4. The (100), (010), (001), (101), (011), (110), (111), (021), (012) and (121) surfaces were investigated in this study had their surface geometry, energy and corresponding electronic structure calculated. The predicted equilibrium and theoretical morphologies of Ag_2SeO_4 were compared with the experimental data. Finally, the relationship between photoluminescence emissions and photocatalytic activity of the as-synthesized materials was analyzed.

Experimental Section

Synthesis

Ag_2SeO_4 samples were synthesized by the SC, UP, CP, and MH methods. Silver nitrate ($AgNO_3$, 99.0%) and sodium selenate ($NaSeO_4$, BioXtra - GHS06, GHS08, GHS09) were purchased from Sigma-Aldrich. In a typical procedure, stoichiometric amounts of Ag^+ and SeO_4^{2-} solutions were prepared by separately dissolving $AgNO_3$ and Na_2SeO_4 in 50 mL of distilled water. Afterwards, both solutions were mixed to form a suspension. In the SC methodology, the suspension was ultrasonicated for 1 h at room temperature in a Branson (model 1510) ultrasonic cleaner, and the crystals were collected after turning off the ultrasonic equipment. In the UP methodology, an ultrasonic probe sonicator (Sonics, GEX 750) was used by inserting the probe into the suspension and maintaining it there for 1 h at room temperature. During CP, the suspension was maintained under stirring at 90 °C for 1 h, and the precipitated was collected after interrupting the stirring. In the MH method, the suspension was transferred to the MH system and maintained at 140 °C for 1 h. Subsequently, all samples were naturally cooled down to room temperature, and the precipitates were separated by centrifugation and washed with deionized water to remove any remaining ions. Finally, the crystals were collected and dried in a conventional an oven at 60 °C for 12 h.

Characterization

The crystals were structurally characterized by X-ray diffraction (XRD) using a D/Max-2000PC Rigaku (Japan) diffractometer with Cu Kα radiation (λ = 1.5406 Å) in the 2θ range from 15° to 60° at a scanning speed of 2°/min in the normal routine, and from 5° to 110° at a scanning speed of 0.2°/min in the Rietveld routine. X-ray photoelectron spectroscopy (XPS) was performed using a Scienta Omicron ESCA+ spectrometer with a high-performance hemispheric analyzer (EA 125) with monochromatic Al Kα (hν = 1486.6 eV) radiation as the excitation source. The operating pressure in the ultrahigh vacuum chamber (UHV) during analysis was $2x10^{-9}$ mbar. Energy steps of 50 and 20 eV were used for the survey and high-resolution spectra, respectively. Micro-Raman spectroscopy was conducted on a Horiba Jobin-Yvon (Japan) spectrometer equipped with a charge-coupled device (CCD) detector and argon-ion laser (Melles Griot, United States) operating at 514.5 nm and a maximum power of 200 mW. Fourier-transform infrared spectroscopy (FTIR) was performed at

room temperature using a Jasco FT/IR-6200 (Japan) spectrophotometer operating in diffuse reflectance mode (DRIFT) with a spectra resolution of 4 cm^{-1} and 32 accumulations per measurement in the range of 400−4000 cm^{-1}. These measurements were carried out on powder mix, which was composed of 1% by weight of each sample mixed with 99% by weight of KBr (99%, Sigma-Aldrich). The shapes and sizes of the crystals were observed on a field emission scanning electron microscope (FE-SEM) model Inspect F50 (FEI Company, Hillsboro, OR) operating at 5 kV. UV-vis diffuse reflectance spectroscopy (UV-vis DRS) was performed using a Varian (USA) spectrophotometer (model Cary 5G) in the diffuse-reflectance mode. Photoluminescence (PL) measurements were carried out at room temperature, with the samples excited by a 355 nm laser (Cobolt/Zouk) focused on a 20-μm spot. The backscattered luminescence was dispersed by a 20-cm spectrometer and the signal was detected by a charge-coupled device detector (Andor technologies).

Theoretical methods and model systems

The theoretical calculations were performed using the CRYSTAL17 package [45] under the framework of well-defined density functional theory (DFT) approximation.

Bulk optimization

For the optimization procedure of the bulk structure, the initial parameters were obtained from the Rietveld experimental values of sample Ag_2SeO_4-MH. All-electron Gaussian-type function basis set Ag+_SC-doll_1998 was used for Ag atom [46], while P_pob_TZVP_2012 was used for Se and O atoms [47]. The exchange and correlation energy was treated within the generalized gradient approximation (GGA) with B3LYP functional [48,49]. An analysis of the band gap values obtained adjusting different percentage of exact Hartree−Fock (HF) exchange for the B3LYP functional was performed and it was found that 25% provides reliable values for both experimental band gap and structural parameters of Ag_2SeO_4. The minimization algorithm chosen was the Broyden–Fletcher–Goldfarb–Shanno (BFGS) scheme [50], and the convergency of energy was set to 10^{-8} Hartree. The shrinking factor (Pack-Monkhorst and Gilat net) was set to 8, which provides an accurate description of the electronic structure. The vibrational modes at the Γ-point were calculated using the numerical second derivate of the total energy. The optimized geometry was obtained by considering a full

optimization, atom coordinates, and cell parameters. The optimized geometry corresponds to a minimum, once all frequencies obtained are positive.

Surface optimization

The (100), (010), (001), (101), (011), (110), (111), (021), (012) and (121) surfaces of Ag_2SeO_4 were represented through slab models using optimized lattice parameters of the bulk. For each surface, there were different possible terminations. The surface energy (E_{surf}) of possible terminated plane was calculated, and the plane with the minimum surface energy was selected as the most thermodynamically stable and used in further surface calculations. The surface energy was calculated as:

$$E_{surf} = \frac{E_{slab} - nE_{bulk}}{2A}, \qquad \text{Eq. 1}$$

where E_{slab} is the total energy of the corresponding slab, n is the number of molecular units present in the slab, E_{bulk} is the energy of the bulk of each polymorph, and 2A corresponds to the area of both sides of the slab. Calculating the E_{surf} values with the Wulff construction results in a polyhedron that depends only on the ratios between the values of the E_{surf} and symmetry point group. [51,52] Convergence energy tests regarding the thickness for symmetrical and stoichiometric slabs were also carried out. Both parameters of 2D slab and number of layers related to the thickness are listed in Table SI-1. By tuning the values of E_{surf}, the available morphologies can be obtained. This methodology provides a simple relationship between E_{surf} and the distance of the planes and has been used in materials science to predict experimental crystal shapes. [52,53]

To rationalize the pathways connecting the different morphologies shapes predicted, the polyhedron energy (E_{poly}) was calculated by summing the contributions of each facet to the morphological shape and the corresponding E_{surf} values, according to the expression:

$$E_{poly} = \sum c_{(hkl)} E_{surf}^{(hkl)} \qquad \text{Eq. 2}$$

where $c_{(hkl)}$ is the percent contribution of the surface area to the total surface area of the polyhedron, and $E_{surf}^{(hkl)}$ is the surface energy of the corresponding surface, according to methodology proposed by our research group. [54]

Electrostatic potential maps were generated with the DFT methodology with the B3LYP and 6-31g(d) functional/basis set combination [55]. Gaussian 09 (https://gaussian.com/glossary/g09/) was used for the numerical data derived from atomic charges of the (001) and (111) surfaces previously optimized to plot the electrostatic potential over the electron density using a color scale RGB (Red, Green and Blue) to represent the potential values. To visualize the electrostatic surface, Jmol software was used (http://www.jmol.org/) considering the values of total charges and a distance of 1.4 Å of the atomic surface.

Photocatalytic measurements

The performance of the as-prepared photocatalysts for the photodegradation of Rhodamine B (RhB) under UV illumination (6 Philips TUV lamps, 15 W) was verified. For this purpose, 50 mg of the photocatalyst and 50 mL of RhB ($1x10^{-5}$ mol/L) were used and placed in ultrasound bath (Ultronique Eco-Sonics, 40kHz) for 5 min. After this step, the photocatalytic solution was transferred to a double-wall sealed cup with a water circulation system maintained at 20 °C and stirred for 30 min to achieve adsorption-desorption balance in the dark. The RhB photodegradation process started by exposing the solution to UV light for 60 min and collecting aliquots at certain times, centrifuging them to remove the catalyst. The remaining solution was analyzed on an UV-vis spectrophotometer (V-660, JASCO) at the maximum RhB wavelength region (λ_{max} = 554 nm). The RhB photodegradation mechanism was investigated through experiments using scavengers of species that may be involved in the reaction, such as p-benzoquinone (BQ 0.012 mol/L), ammonium oxalate (AO 0.012 mol/L), and tert-butyl alcohol (TBA 0.012 mol/L) as scavengers of superoxide radical (O_2'), hole ($h^{\bullet}$), and hydroxyl radical (OH*), respectively.

Results and Discussion

XRD and Rietveld refinement

The XRD patterns of the Ag_2SeO_4 samples obtained by different methods are presented in Fig. 1. It is possible to observe that all diffractograms contain prominent and clearly distinguishable peaks perfectly indexed to crystalline Ag_2SeO_4 orthorhombic phase and space group *Fddd* (Z = 8), according to ICSD no. 41-3089. [31,41] Secondary phases and impurities peaks cannot be identified, confirming the purity and

high crystallinity of the samples, as well as their structural long-range order irrespective of the synthesis methods.

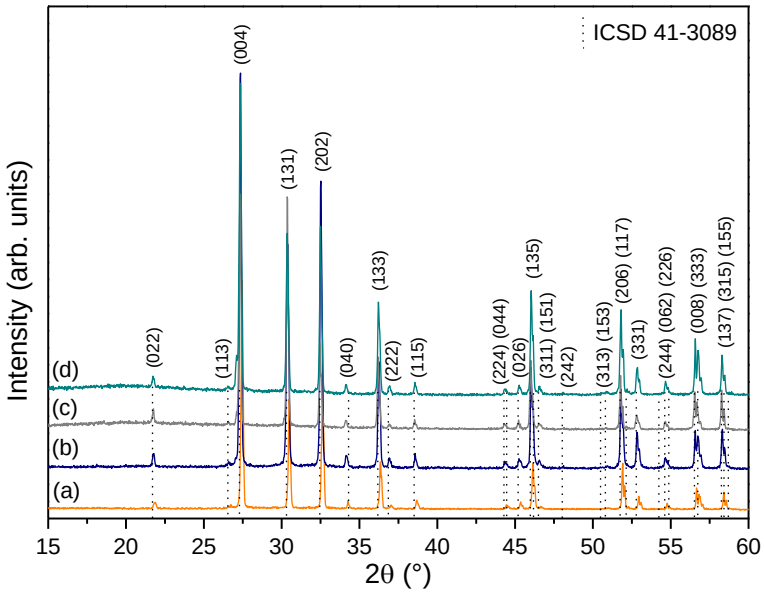

Figure 1. XRD patterns of samples (a) Ag_2SeO_4-SC, (b) Ag_2SeO_4-UP, (c) Ag_2SeO_4-CP, and (d) Ag_2SeO_4-MH

The structural properties of the Ag_2SeO_4 samples were investigated by Rietveld refinement using the general structure analysis system (GSAS) software. [56] The refined parameters were preferred orientation, lattice parameters, shift lattice constants and atomic functional positions among other instrumental and sample parameters. The background was adjusted by a Chebyshev function, while the peak profile was fitted by a convolution of Thompson-Cox-Hastings pseudo-Voigt (pV-TCH) function. The asymmetry function and the anisotropy in the half-width of the reflections were determined according to Finger et al. [57] and Stephens [58], respectively. ~~In addition, experimental lattice parameters, unit cell volume, statistical parameters of quality (χ^2 and R_{Bragg}) and atomic positions of the Ag_2SeO_4 microcrystals were also performed.~~ Figs. SI-1(a–d) show the Rietveld refinement plot of the Ag_2SeO_4 microcrystals obtained by different synthesis methods. Table 1 summarizes the experimental and theoretical data from the Rietveld refinement analysis, including lattice parameters, cell volume and statistical parameters (χ^2 and R_{Bragg}). The results show that all samples present similarity to the ICSD No. 41-3089, and all synthesis methods are efficient to obtain the materials without high degree of structural disorder. Additionally, Table SI-2 presents the atomic coordinates (x, y, z) for Ag, Se and O atoms, while Table SI-3

shows the crystallographic data of the Rietveld refinement. All data reveal a good fit between the calculated and observed XRD patterns, indicating satisfactory values for a quality refinement.

Table 1. Lattice parameters, unit cell volume and statistical parameters of quality obtained by Rietveld refinements of Ag_2SeO_4 microcrystal obtained by SC, UP, CP and MH methods

Refined formula Ag_2SeO_4	Lattice Parameters (Å)			Cell volume (Å^3)	R_{Bragg} (%)	χ^2 (%)
	a	b	c			
Ag_2SeO_4-SC	6.05142(7)	10.39899(16)	12.98369(11)	817.047(16)	3.15	1.22
Ag_2SeO_4-UP	6.05279(10)	10.40138(24)	12.98497(16)	817.499(26)	3.59	1.34
Ag_2SeO_4-CP	6.05335(17)	10.39740(25)	12.98864(18)	817.493(32)	4.18	1.35
Ag_2SeO_4-MH	6.05196(10)	10.39745(23)	12.98219(13)	816.903(24)	3.31	1.27
Ag_2SeO_4-Theo	6.139	10.928	12.974	873.744	-	-
ICSD No. 41-3089	6.0531(9)	10.3898(11)	13.0001(11)	817.58	-	-

A representation of the unit cell for the orthorhombic Ag_2SeO_4 structure can be seen in Fig. 2. The unit cell was modeled in VESTA (Visualization for Electronic Structural Analysis) software [59,60] using lattice parameters and atomic positions obtained from the Rietveld refinement data and the optimized structure of the theoretical calculation (Ag_2SeO_4-Theo). Based on the structure optimization of Ag_2SeO_4, the lattice parameters obtained were found to be in good agreement with the experimental values of sample Ag_2SeO_4-MH (see Table 1), meaning that our calculation methods are reasonable and that the calculated results are authentic. In this system, the Ag coordination environment is a distorted oxygen octahedron, $[AgO_6]$, with three pairs of $Ag-O$ bond lenghts of 2.378, 2.543 and 2.783 Å, while Se is at the center of a distorted tetrahedron, $[SeO_4]$, with $Se-O$ bond length of 1.686 Å. Therefore, as the bond lengths of $Ag-O$ are larger than that of $Se-O$, the interaction between Se and O atoms is relatively stronger than that between Ag and O atoms in the orthorhombic Ag_2SeO_4.

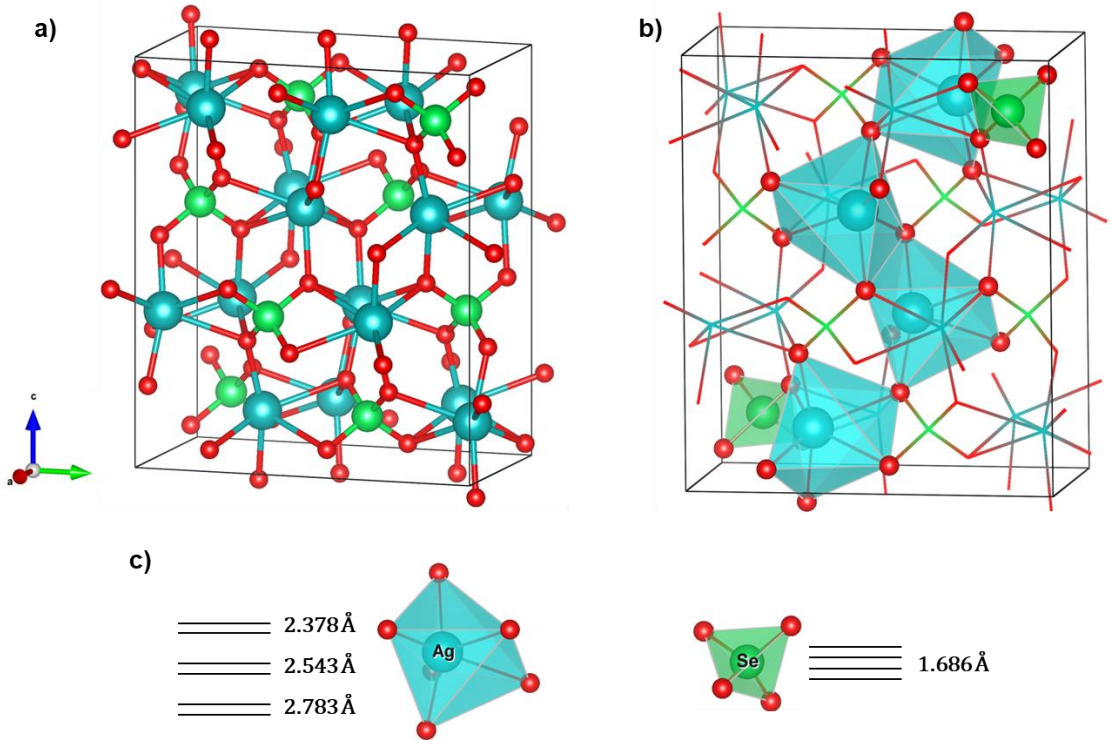

Figure 2. Unit cell representation of the Ag_2SeO_4 microcrystal. (a) Ball-stick model, (b) polyhedral AgO_6 and SeO_4 models, and (c) $Ag-O$ and $Se-O$ bond lengths represented by horizontal lines. Cyan, green, and red balls represent Ag, Se and O atoms, respectively.

XPS

XPS analysis was carried out to provide information about the chemical composition, binding energy, atomic bonding configuration, electronic structure, and oxidation states of the constituent atoms on the surface of Ag_2SeO_4 samples. The survey XPS spectra of the Ag_2SeO_4 samples are displayed in Fig. 3, where the C, Ag, Se, and O peaks for all samples and no other elements due to impurities can be identified.

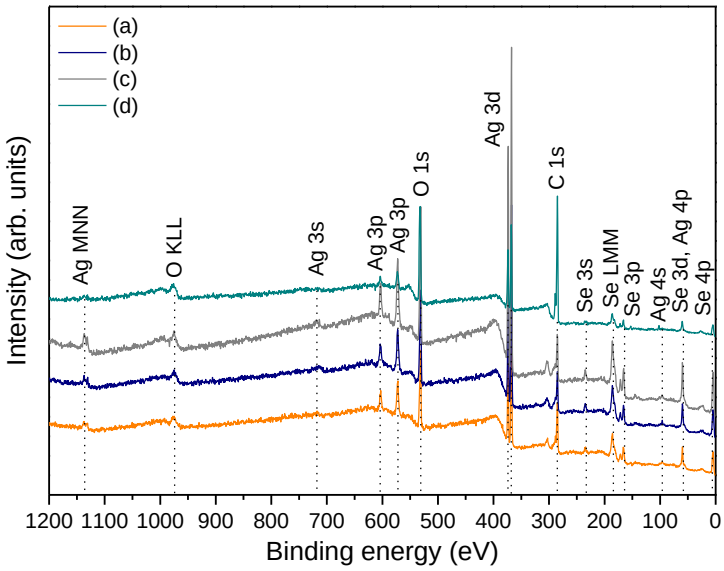

Figure 3. XPS spectra of samples (a) Ag_2SeO_4-SC, (b) Ag_2SeO_4-UP, (c) Ag_2SeO_4-CP, and (d) Ag_2SeO_4-MH

Figs. SI-2(a-d) show the Ag 3d spectra in the range of 380-364 eV. Two deconvolution components located around 367.3 and 373.3 eV (Δ = 6 eV) are attributed to Ag $3d_{5/2}$ and Ag $3d_{3/2}$, respectively, confirming the presence of the Ag^+ ion. Also, other two deconvolution components around 368.1 and 374.1 eV(Δ = 6 eV) indicate the presence of Ag^0, which can be related to the surface coating of Ag nanoparticles on the material surface. [61–65] Figs. SI-3(a-d) display the Se 3p spectra in the range of 178-156 eV. The spectra present doublet Se 3p peak around 165.6 eV (Se $3p_{3/2}$) and 171.3 eV (Se $3p_{1/2}$), evidencing the Se(VI) oxidation state. For the Ag_2SeO_4-MH, one extra peak at 160.3 eV ascribed to Se^0 is observed because of the MH conditions, which favor the reduction of Se(VI). [66–71] Figs. SI-4(a-d) show the O 1s spectra in the range of 538-528 eV. The spectra present three main spin-orbit components around 530.8, 532.3 and 533.8 eV. Generally, the component located at 530.8 eV is attributed to lattice oxygen, which corresponds to Ag–O and Se–O bonds, being related to the host lattice of the materials. The component at 532.3 eV is assigned to oxygen vacancies, which have a greater contribution in sample Ag_2SeO_4-MH due to the reduction of Se(VI). Finally, the component at 533.8 eV corresponds to OH groups and water adsorbed on the surface of the materials. [72–78] Table SI-4 lists the positions of the XPS elements and the concentration of the area components for the elements Ag, Se and O of the Ag_2SeO_4 samples. The aforementioned results prove the existence of such elements as well as the purity of the sample surface.

Raman

Fig. 4 shows the Raman spectra at room temperature of Ag_2SeO_4 samples excited by a green laser. According to group theory analysis, the *Fddd* structure of Ag_2SeO_4 has 42 Raman and infrared active modes, as stated by the following irreducible representation: $\Gamma = 4A_g + 6B_{1g} + 6B_{2g} + 5B_{3g} + 4A_u + 6B_{1u} + 6B_{2u} + B_{3u} + 5B_{3u}$. The active Raman modes were experimentally observed at 98, 322, 348, 394, 416, 437, 812 and 847 cm^{-1}, and are close to the theoretical modes predicted, as shown in Table 2. Peaks below 300 cm^{-1} are common and can be ascribed to lattice modes. For this system, one peak at 98 cm^{-1} was identified, being also present in other related materials such as Na_2SeO_4. [39] Peaks above 300 cm^{-1} can be related to internal vibrations of the tetrahedral SeO_4^{2-} (point group T_d), which split into seven Raman active modes in the orthorhombic crystal environment. Among them, the most intense peak at 812 cm^{-1} can be attributed to the symmetric vibration of the selenate tetrahedron. [40] Some small differences observed are due to changes in the reduced masses and bonding strengths of the Ag_2SeO_4. These results confirm the structural short-range order of all samples and the crystallization of the materials regardless of the method of synthesis used.

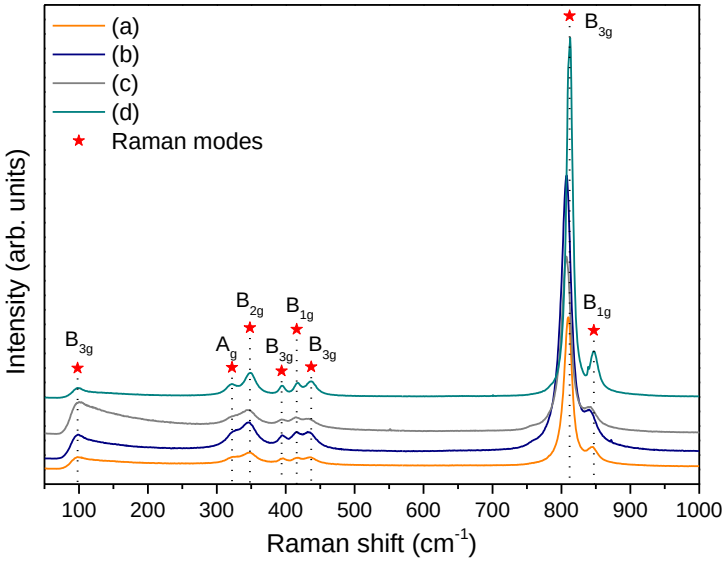

Figure 4. Raman spectra of samples (a) Ag_2SeO_4-SC, (b) Ag_2SeO_4-UP, (c) Ag_2SeO_4-CP, and (d) Ag_2SeO_4-MH

Table 2. Experimental and theoretical values of Raman and IR vibrational frequencies of Ag_2SeO_4

Position (cm^{-1})					
Raman			IR		
Modes	**Experimental**	**Theoretical**	**Modes**	**Experimental**	**Theoretical**
B_{3g}	98	104	B_{1u}	420	380
A_g	322	325	A_u	669	682
B_{2g}	348	374	B_{1u}	820	792
B_{3g}	394	409	B_{3u}	843	796
B_{1g}	416	418	B_{2u}	873	821
B_{3g}	437	452	-	-	-
B_{3g}	812	837	-	-	-
B_{1g}	847	838	-	-	-

FTIR

The FTIR spectra of the Ag_2SeO_4 samples are presented in Fig. 5, whereas the experimental and theoretical calculated IR bands are listed in Table 2. The band appearing around 420 cm^{-1} can be assigned to the O-Se-O asymmetric bonding mode. The mode at 669 cm^{-1} can be attributed to the symmetric and asymmetric stretching modes of Se-O. [79,80] The splitting band (820, 843 and 873 cm^{-1}) with the most intense peak at 843 cm^{-1} is ascribed to the ~~infrared-active~~ Se-O stretching mode. [40,81] The 900-4000 cm^{-1} region of the spectra typically present characteristic bands of CO_2 and H_2O due to room atmosphere and humidity. The modes at 1633 and 1677 cm^{-1} correspond to the bending vibration band of molecular H_2O. The weak mode around 3400 cm^{-1} is related to O-H stretching modes of the adsorbed H_2O. [81–84] These FTIR modes attest the structural order of all samples and are in agreement with the theoretical values listed in Table 2.

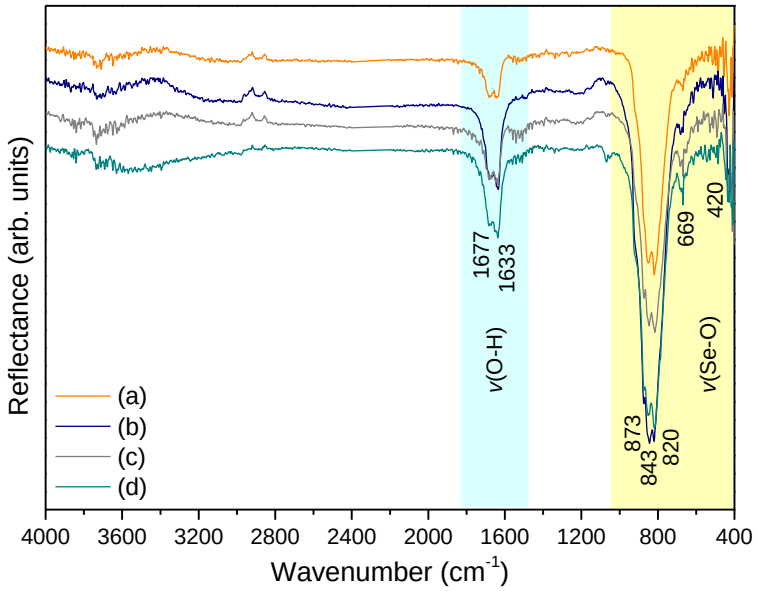

Figure 5. FTIR spectra of samples (a) Ag_2SeO_4-SC, (b) Ag_2SeO_4-UP, (c) Ag_2SeO_4-CP, and (d) Ag_2SeO_4-MH

UV-vis spectroscopy

Fig. 6(I) displays the UV-vis diffuse reflectance spectra of the Ag_2SeO_4 samples within the range of 300-750 nm. It can be seen that the samples show absorption in the ultraviolet region at approximately 400 nm as a result of the electronic transition between the valence band (VB) formed by the hybridization of Ag 5d and the O 2p orbitals, and the conduction band (CB) formed by Ag 5s and Se 4p orbitals. The band gap energy (E_{gap}) values were calculated using the Kubelka-Munk function and Wood Tauc plot, and obtained by the linear extrapolation of the UV-vis curves in the $[F(R_\infty)h\upsilon]^n$ *versus* $h\upsilon$ graph, where $F(R_\infty)$ is the Kubelka-Munk function [85], $h\upsilon$ is the photon energy, and n is a constant related to the type of electronic transition of a semiconductor (n = 0.5 for direct allowed, n = 2 for indirect allowed, n = 1.5 for direct forbidden, and n = 3 for indirect forbidden). The theoretical calculation predicted an indirect allowed transition for Ag_2SeO_4 with the space group *Fddd*. The E_{gap} values obtained were 2.86, 2.88, 2.87 and 2.88 eV for samples Ag_2SeO_4-SC, Ag_2SeO_4-UP, Ag_2SeO_4-CP and Ag_2SeO_4-MH, respectively (Fig. SI-5). These results are similar to those found in the literature [86] and show similar E_{gap} values for all crystals, indicating that the degree of order-disorder at the electronic level was not affected by the synthesis method. It means that intermediary energy levels were not created within the band gap due to the defects in the structure.

The electronic structure of Ag_2SeO_4 was obtained by DFT calculations, including band structure, density of states (DOS) and partial density of states (PDOS). The band structure plot using five high symmetry lines of the Brillouin zone is shown in Fig. 6(II). It can be seen that the VB is flat and according to our assignment of the *k*-points, with the valence band maximum (VBM) located along the $\Gamma - X$ point, while the CB is more dispersive, with the conduction band minimum (CBM) located at the Γ point. Based on the calculated band structure, Ag_2SeO_4 is a semiconductor with indirect band gap and a calculated E_{gap} value of 2.89 eV that coincides with the experimental optical E_{gap} (Fig. SI-5). The VBM and its vicinity are mainly composed of Ag 5*d* orbitals with significant contribution of O *2p* orbitals. The analysis of the VB region indicates the presence of Ag 5*s* and Ag *5d* states along the evaluated energy range. The CBM, on the other hand, is predominantly formed by Ag 5*s* states as well as contributions of Se *4s* and O 2*p* states (Fig. 6(III)).

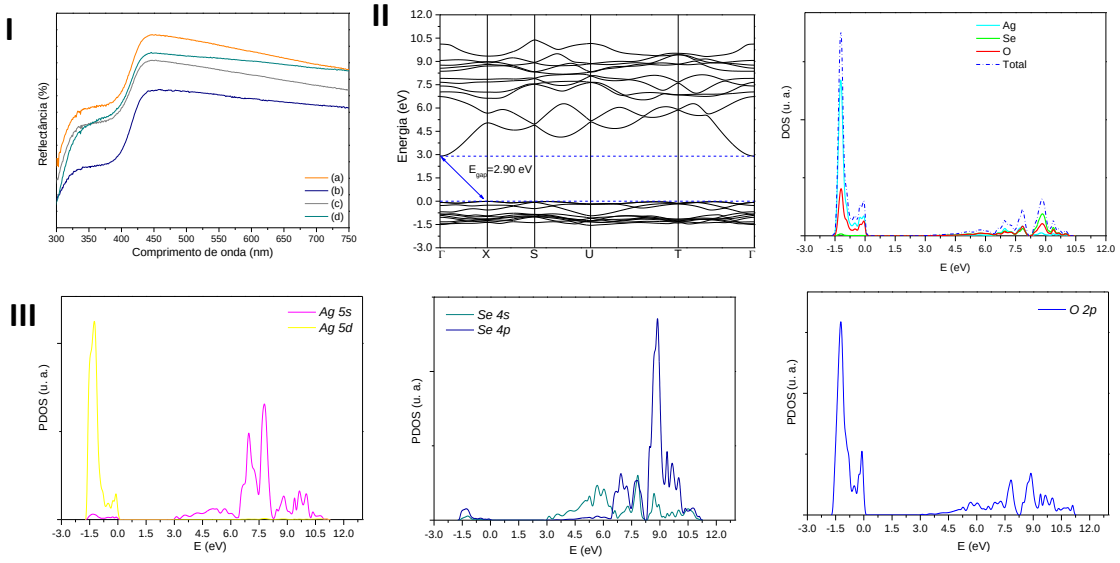

Figure 6. (I) UV-vis diffuse reflectance spectra of samples (a) Ag_2SeO_4-SC, (b) Ag_2SeO_4-UP, (c) Ag_2SeO_4-CP, and (d) Ag_2SeO_4-MH. (II) Structure band and DOS, and (III) PDOS calculated by DFT.

FE-SEM

The FE-SEM micrographs of the Ag_2SeO_4 samples are shown in Fig. 7, where it is possible to observe faceted block-like particles with a high degree of heterogeneity in shape and size. Additionally, the particles present smooth surface, well-defined shapes, and are mainly aggregated with a polydisperse size distribution.

Figs. 7(a, b) show the FE-SEM images of sample Ag_2SeO_4-SC, where rhombus-shaped crystals of different sizes ranging from 1 to 6 μm can be clearly seen. Some of them have truncated face and flat morphology, while others present deformed shapes with lengths larger than widths, resulting in rod-like crystals. Crystals with a well-defined truncated hexagonal plate morphology are predominantly observed in sample Ag_2SeO_4-UP, as illustrated in Figs. 7(c, d). It is also possible to note morphologies of various truncated octagonal rods and truncated rhombic shapes, with many of them in process of formation. Figs. 7(e, f) show octahedral microcrystals with triangular faces ascribed to Ag_2SeO_4-CP, being these morphologies similar to the ones observed in $ZnMoO_4$. [87] Moreover, there are some deformed rods with hexagonal and cubic faces. Figs. 7(g, h) show the crystal Ag_2SeO_4-MH, which is mainly composed of truncated cubes, in addition to rhombus crystals and rods with flat and elongated shapes. These results confirm that Ag_2SeO_4 can be synthesized by different methods and that various morphologies can be obtained without the use of surfactants, templates, organic solvents, or medium pH adjustment. Particularly, each synthesis method provides distinct forces of interaction (temperature, sonication, physic stirring, pressure, microwave radiation) for the [AgO_6] and [SeO_4] clusters, which account for the overall energy of the system, thus resulting in different morphologies observed. Also, these results reveal that morphology control can provide a great versatility for tuning and enhancing the applications of materials.

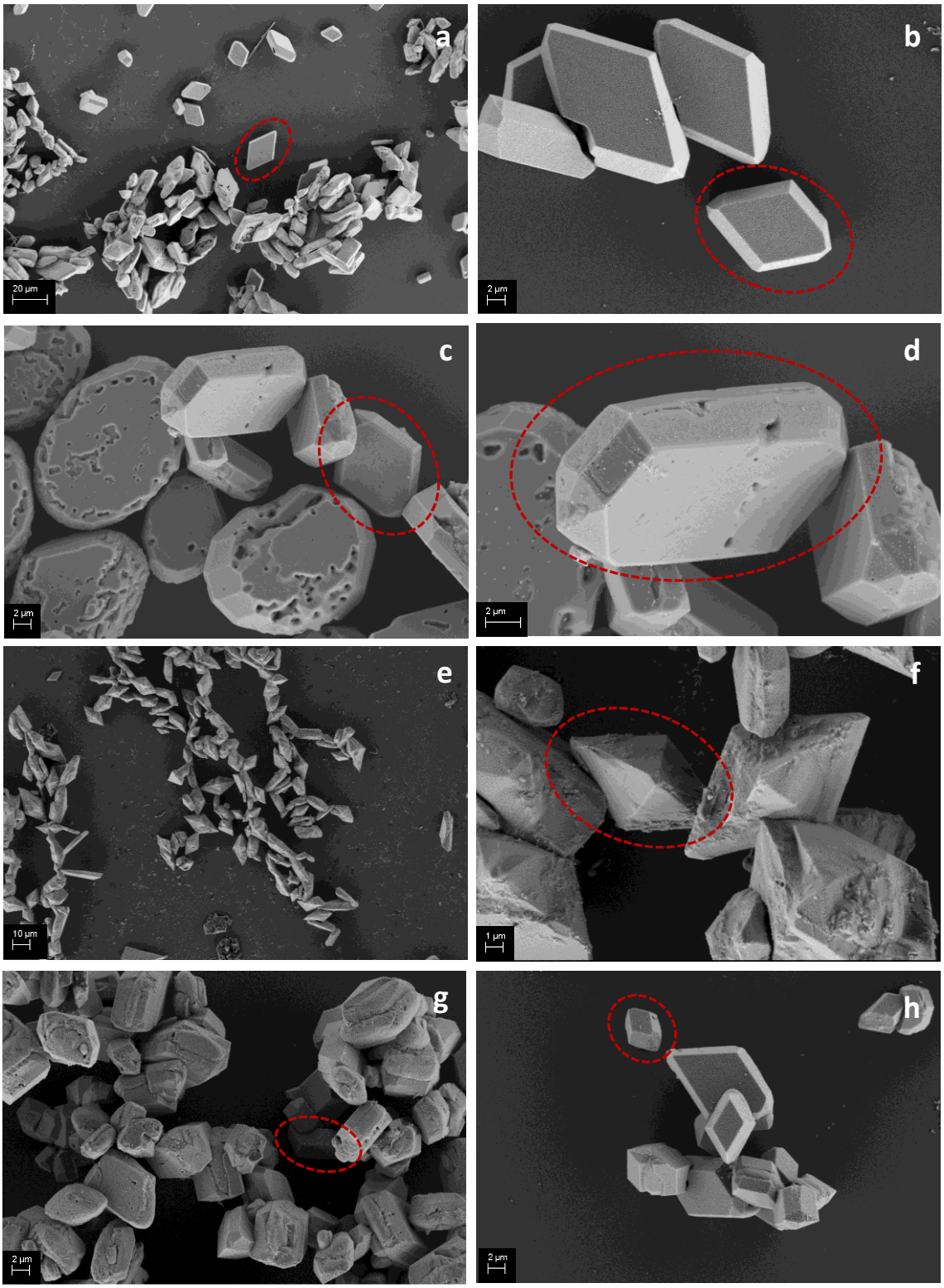

Figure 7. FE-SEM images of samples (a,b) Ag_2SeO_4-SC, (c,d) Ag_2SeO_4-UP, (e,f) Ag_2SeO_4-CP, and (g,h) Ag_2SeO_4-MH

In order to characterize the surfaces and describe the morphologies experimentally obtained, a set of possible theoretical morphologies were obtained from the calculated E_{surf} values via the Wulff construction. The surfaces modeled from the optimized bulk of Ag_2SeO_4 are displayed in Fig. 8, whereas their calculated E_{surf} values after relaxation are listed in Table 3. The results in Table 3 reveal that (111) is the most stable surface with the lowest E_{surf} (0.19 Jm^{-2}), followed by the (010)/(001) and (011) surfaces, which have approximately the same E_{surf} value (0.22 and 0.23 Jm^{-2}, respectively). The set of Wulff constructions obtained by tuning the relative stability of the calculated surfaces is presented in Fig. SI-6, while the theoretical morphologies associated with the experimentally obtained data are illustrated in Fig. 9.

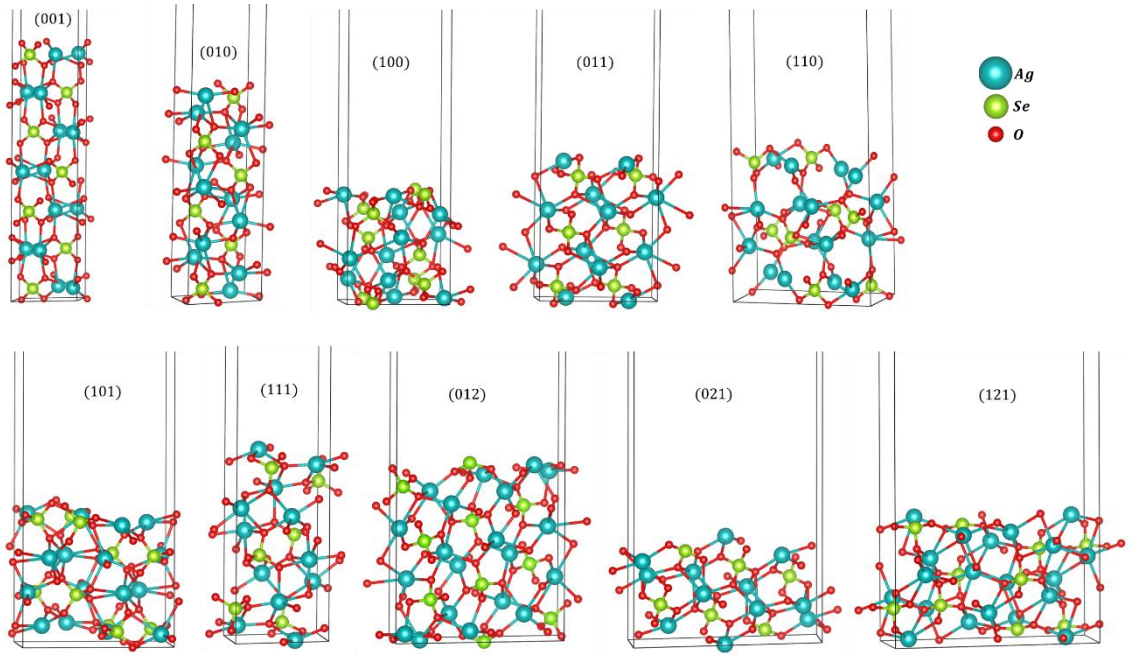

Figure 8. Geometric structure of the surface models of Ag_2SeO_4. Cyan, green and red balls represent Ag, Se and O atoms, respectively

Table 3. Surface area (A, nm^{-2}), surface energy (E_{surf}, Jm^{-2}), number of dangling bonds (N_B) and surface densities of dangling bonds (D_B, nm^{-2}) of the Ag_2SeO_4 surfaces

Surface	A	E_{surf}	N_B	D_B
(100)	0.709	0.93	8	11.28
(010)/(001)	0.39/0.33	0.22	4/4	11.92/10.04
(101)	0.78	0.28	6	7.65
(011)	0.52	0.23	6	11.52
(110)	0.81	0.34	14	17.22
(111)	0.44	0.19	3	9.09
(012)	0.78	0.64	7	6.26
(021)	0.86	0.54	9	11.53
(121)	0.11	0.61	8	9.26

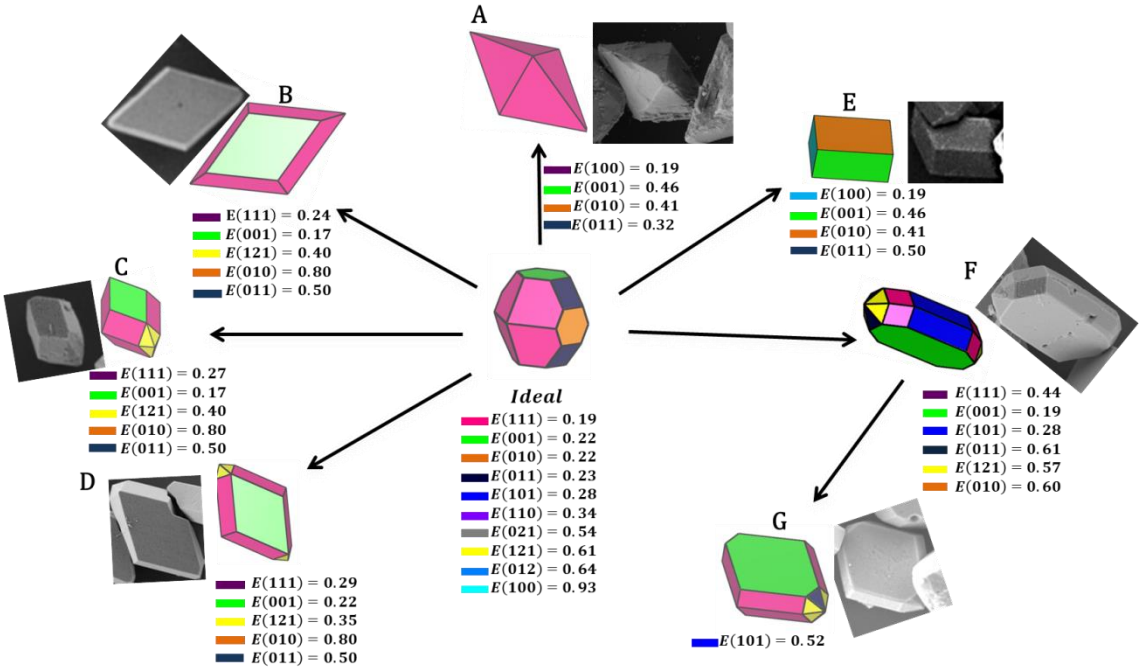

Figure 9. Crystal shape computationally simulated for Ag_2SeO_4 synthesized by SC, UP, CP, and MH methods. The experimental shapes are included for comparison. Surface energy values are given in Jm^{-2}

The thermodynamically stable macroscopic crystal shape of Ag_2SeO_4 was determined according to the E_{surf} values of Table 3 using the VESTA software [59]. For the Ag_2SeO_4 crystal, four facets [(111), (010), (001) and (011)] are exposed to the vacuum, forming a truncated octahedron. Usually, the lower the energy of a surface, the more it contributes to the crystal shape. In this case, the most stable surface, i.e., (111), covers about 63.07% of the total crystal shape area, while the (010), (001) and (011) surfaces respectively correspond to 9.84%, 14.29% and 18.84 % of the total crystal shape area. Table SI-5 presents the contribution of each surface to the total crystal shape as well as their relative energy.

The results reveal that the octahedral microcrystals with triangular faces (morphology A in Fig. 9) obtained by the CP method is the most stable and with stability rather similar to the ideal morphology (see Fig. 10). While morphology A exposes exclusively the (111) surface and is obtained by destabilizing the E_{surf} of the (001) surface, the E_{surf} of the former surface remains unchanged.

The rhombus morphologies of different sizes observed in the synthesis by SC and MH are described mainly by the (001) and (111) surfaces. The flat rhombic shape (morphology B in Fig. 9) appears due to the increase in the E_{surf} of the (010) and (011) surfaces and the stabilization of the (001) surface, which in turn increase the E_{poly}. On the other hand, in the truncated rhombic shape (morphologies C and D in Fig. 9) there are smaller contributions of the (121) surface to the total morphology. The truncated rhombic shape obtained by the SC method exposes the (111) surface in minor proportion compared to the MH method. An opposite behavior is observed for the (121) surface, but with equal E_{poly} values for morphologies C and D. This can be understood as a competitive effect of stability between both surfaces, as indicated in Table SI-5.

It can be seen that morphology E (Fig. 9) obtained by the MH method exposes the three lowest index surfaces, that is, (100), (010) and (001). To obtain this morphology, it is necessary to increase the E_{surf} value of the (001), (011) and (111) surfaces to 0.30, 0.80 and 0.80 Jm^{-2}, respectively. The destabilization of these surfaces promotes the exposure of the (101) and (110) surfaces, thus requiring an increase in the relative energy values of these surfaces to 0.55 Jm^{-2} and the simultaneous stabilization of the most unstable (100) surface, reducing its E_{surf} value to 0.40 Jm^{-2}.

The synthesis by the UP method resulted in morphologies F and G (Fig. 9). Crystal morphology F is characterized by the (001), (101), (011), (111) and (121) surfaces, with predominance of the two first. Initially, the UP method is able to promote

the exposure of the (101) surface through the destabilization of the (011) and (111) surfaces by increasing the values of the E_{surf} to 0.61 and 0.44 Jm^{-2}, respectively. Simultaneously, the E_{surf} values for the (001) and (121) surfaces are reduced to 0.19 and 0.40 Jm^{-2}, respectively. Regarding the obtention of morphology G, an increase in the E_{surf} of the (101) surface is needed, as shown in Fig. 9. In addition, as illustrated in Fig. 10 these morphologies have higher values of E_{poly} than the ideal morphology, as they are generated by the destabilization of the surfaces involved in the process.

Finally, with exception of morphology E, the most stable (111) and (001) surfaces are present in all obtained morphologies. Also, a rhombus morphology as a result of the SC, UP and MH methods is obtained with minimum changes in the E_{surf} value compared with the ideal morphology. However, when obtained by the UP method the rhombic shape exposes the (011) surface, but not when obtained by other methodologies.

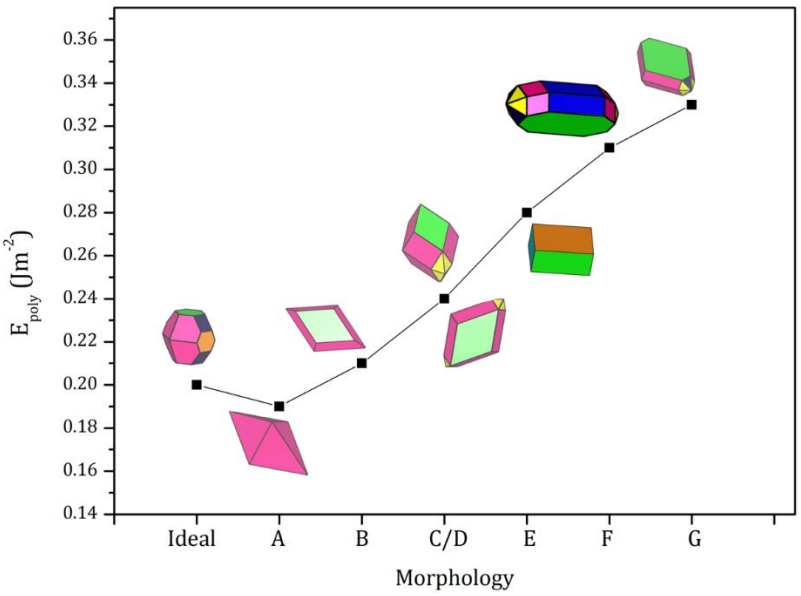

Figure 10. Polyhedron energy profile connecting the ideal and associated morphologies to the experimentally obtained data

Surface geometric and electronic structures

Based on the optimized structural parameters, the structural and electronic properties of the different surfaces of Ag_2SeO_4 were investigated. The clusters of the unsaturated Ag and Se atoms exposed on the surfaces of the samples and the corresponding neutral oxygen vacancies (V_o^x) were described by using the Kröger–Vink notation [88]. Because of the weak symmetry breaking in the *b*-*c* plane, there are

only slightly differences between the geometric structures of the (010) and (001) surfaces of Ag_2SeO_4. Thus, physical properties such as surface electronic structures and surface energies are expected to be similar, which means that the discussion presented for the (010) surface is also valid for the (001). It is also concluded that except for the (100), all surfaces with index *hkl* < 2 are terminated with saturated Se atoms, i.e., $[SeO_4]$ clusters.

(100) surface. The relaxed structure of the (100) surface is shown in Fig. SI-7(a). It can be seen that the (100) surface exposes three unsaturated Ag atom, being two of them fourfold coordinated and forming the equivalent undercoordinated $[AgO_4 \cdot 2V_O^x]$ clusters, while the other one is fivefold coordinated, resulting in the undercoordinated $[AgO_5 \cdot V_O^x]$ cluster. Both four- and fivefold undercoordinated clusters present $Ag-O$ with average bond length of 2.401 Å. In addition, two undercoordinated $[SeO_2 \cdot 2V_O^x]$ clusters are also present in this surface. The $Se-O$ surface bonds have equal length of 1.685 Å. Fig. SI-7(b) shows the DOS of the surface atoms in the relaxed (100) surface slab. The value of the calculated E_{gap} for this surface is 0.47 eV. The sharp peaks are mainly composed of O 2*p* and Se 4*s* located in the bulk band gap region.

(010) and (001) surfaces. The relaxed geometric structure of the (010)/(001) surfaces is illustrated in Fig. SI-7(c). The surfaces present two fourfold coordinated Ag atoms, indicated as undercoordinated $[AgO_4 \cdot 2V_O^x]$ clusters. The $Ag-O$ bond lengths are different in each of these clusters and separated into two groups of two, with bond length values of 2.227 and 2.796 Å in one, and 2.462 and 2.341 Å in the other. The $Se-O$ bond lengths in the $[SeO_4]$ clusters are also separated into two groups of two, with values of 1.673 and 1.698 Å, but they are different from the bulk, which has four $Se-O$ bonds with equal length. Fig. SI-7(d) shows the DOS of the surface atoms in the relaxed (001) surface slab. It is possible to note that the value of the calculated E_{gap} is 2.97 eV and that the surface Fermi level almost coincides with that of the bulk. The VB region is described by only one sharp peak composed of O 2*p* and Ag 5*d* states and hybridized states at approximately 0.5 eV, while the CB region presents Se 4*s* and O 2*p* hybridized states.

(101) surface. The (101) surface exposes two coordinated Ag atoms separated into two group of clusters: two undercoordinated $[AgO_5 \cdot V_O^x]$ and two $[AgO_4 \cdot 2V_O^x]$ clusters (Fig. SI-7(e)). The two undercoordinated $[AgO_5 \cdot V_O^x]$ clusters are equivalent to each other, as are the undercoordinated $[AgO_4 \cdot V_O^x]$ clusters. The five $Ag-O$ bond

lengths in the $[AgO_5 \cdot V_O^x]$ clusters are different, varying from 2.331 to 2.838 Å. The tetrahedral $[AgO_4 \cdot 2V_O^x]$ cluster are formed by four $Ag-O$ bonds with lengths varying from 2.296 to 2.577 Å. The $Se-O$ average bond length is 1.70 Å, similar to the bulk value. Fig. SI-7(f) shows the DOS of the surface atoms in the relaxed (101) surface slab. The value of the calculated E_{gap} for this surface is 3.12 eV, which is slightly higher than that of the bulk. The VB region is mainly described by O 2*p* states, while the CB presents dispersed states with small contributions of O 2*p* and Se 4*s* orbitals.

(011) surface. The (011) surface exposes two threefold coordinated Ag atoms (Fig. SI-8(a)), generating two equivalent planar undercoordinated $[AgO_3 \cdot 3V_O^x]$ clusters with $Ag-O$ bond lengths of 2.227, 2.267 and 2.446 Å. The surface $[SeO_4]$ cluster present in this surface is formed by a $Se-O$ bond with length of 1.680 Å. Fig. SI-8(b) shows the DOS of the surface atoms in the relaxed (011) surface slab. The value of the calculated E_{gap} for this surface is 3.12 eV, which is slightly higher than that of the bulk. The VB region is described by O 2*p* and Ag 5*d* states, while the CBM presents minimum contributions of O 2*p* states.

(110) surface. This surface presents four unsaturated Ag atoms separated into two groups of two, as illustrated in Fig. SI-8(c). The undercoordinated $[AgO_3 \cdot 3V_O^x]$ clusters are composed of $Ag-O$ bonds with lengths of 2.227, 2.267 and 2.446 Å, whereas the $[AgO_2 \cdot 4V_O^x]$ clusters are formed by $Ag-O$ bonds with lengths of 2.158 and 2.163 Å. The $[SeO_4]$ clusters exposed at the top surface are symmetrically equivalent and have three different $Se-O$ bonds with lengths of 1.658, 1.687 and 1.693 Å. Fig. SI-8(d) shows the DOS of the surface atoms in the relaxed (110) surface slab. The value of the calculated E_{gap} for this surface is 3.18 eV, which is close to that of the bulk. The VB region is mainly composed of O 2*p* states with minor contribution of Ag 5*d* states. There are no states in the band gap region.

(111) surface. The relaxed structure of the (111) surface is shown in Fig. SI-8(e), where it is possible to see two fourfold coordinated Ag surface atoms forming two distorted tetrahedral undercoordinated $[AgO_4 \cdot 2V_O^x]$ clusters with $Ag-O$ average bond lengths of 2.432 and 2.455 Å, which are shorter than the bulk values. The $[SeO_4]$ surface cluster has $Se-O$ average bond length of 1.683 Å. Fig. SI-8(f) shows the DOS of the surface atoms in the relaxed (111) surface slab. In the VB region, peaks observed in the energy range of -1.5 to 0 eV are due to Ag-5*d* and O 2*p* states. The E_{gap} of 2.97 eV obtained through the DOS plot is close to the bulk value (2.90 eV). This result is

expected because the (111) surface presents the highest contribution to the total crystal area and no states occur in the band gap region of the material.

(012) surface. Fig. SI-9(a) shows the relaxed geometric structure of the (012) surface, where four Ag atoms and one Se atom are observed. Of the four Ag atoms, two are fivefold and two are threefold coordinated, while the Se atom is also threefold coordinated. The undercoordinated $[AgO_5 \cdot V_O^x]$ clusters have five different $Ag-O$ bonds with lengths from 2.270 to 2.740 Å, whereas the undercoordinated $[AgO_5 \cdot V_O^x]$ clusters have $Ag-O$ bonds with lengths ranging from 2.410 to 2.426 Å. The undercoordinated $[SeO_3 \cdot V_O^x]$ clusters have three different $Ag-O$ bonds with lengths of 1.677, 1.710 and 1.788 Å, which are on average higher than that of the bulk. The calculated E_{gap} is 2.10 eV, which is lower than the bulk value, indicating that states located in the band gap region of the bulk are expected, being them mainly composed of O 2*p* (Fig. SI-9(b)).

(021) surface. The relaxed (021) surface illustrated in Fig. SI-9(c) exposes two fivefold and two threefold coordinated Ag atoms, while the exposed Se atom is threefold coordinated. The undercoordinated $[AgO_5 \cdot V_O^x]$ clusters have $Ag-O$ bonds with lengths from 2.383 to 2.781 Å, whereas the undercoordinated $[AgO_3 \cdot 3V_O^x]$ clusters have bond lengths of 2.383 and 2.538 Å. The undercoordinated $[SeO_3 \cdot V_O^x]$ clusters present three equal bond lengths of 1.680 Å. The calculated E_{gap} for this surface is 1.87 eV (Fig. SI-9(d)), which is lower than that of the bulk. The CBM is composed of O 2*p* and Ag 5*s* orbitals.

(121) surface. Fig. SI-9(e) shows that the (121) surface presents four unsaturated Ag atoms, where two kinds of Ag clusters can be found: undercoordinated $[AgO_5 \cdot V_O^x]$ and $[AgO_4 \cdot 2V_O^x]$ clusters. The $Ag-O$ bonds in the undercoordinated $[AgO_5 \cdot V_O^x]$ clusters are separated into two groups of two, with lengths of 2.383 and 2.538 Å, plus one $Ag-O$ bond with length of 2.781 Å. In the undercoordinated $[AgO_4 \cdot 2V_O^x]$ clusters, the $Ag-O$ bonds are also separated into two groups of two, with lengths of 2.0538 and 2.781 Å. Additionally, two threefold Se atoms are exposed in this surface, and the undercoordinated $[SeO_3 \cdot V_O^x]$ clusters have bond length of 1.680 Å. According to Fig. SI-9(f), the calculated E_{gap} for this surface is 1.23 eV. The peak located in the band gap region of the bulk is generated by O 2*p* and Ag 5*s* states as well as Se 4*s* states.

Undercoordinated Ag clusters do not generate states in the band gap region of the bulk. However, the presence of undercoordinated Se clusters on the surface leads to the appearance of O 2*p* and Ag 5*s* states, causing the surface E_{gap} value to be lower than that of the bulk. Surfaces terminated in Se clusters with the lowest coordination number have the lowest E_{gap} values. From undercoordinated clusters presented at the top of each surface it is possible to obtain the number of the dangling bonds (N_B), and then calculate their density ($D_B = N_B/A$, where N_B is the total number of $Ag - O$ and $Se - O$ dangling bonds), which is associated with the structural order-disorder degree in the referred region. These values are listed in Table 3. The calculated D_B defined the following structural order at the top surfaces: (012) > (101) > (111) > (121) > (001) > (100) < (011) ~ (021) > (010) > (110), with values of 6.26, 7.65, 9.09, 10.04, 11.28, 11.52, 11.53, 11.92 and 17.22 nm^{-2}, respectively. Therefore, it can be concluded that the (012) is the most organized surface, while the (110) is the less organized one.

Photoluminescence spectroscopy

Fig. 11(a) shows the PL emission spectra at room temperature of the Ag_2SeO_4 samples under the excitation wavelength of 355 nm. All spectra present a broadband profile covering the entire visible region, with maximum PL intensity at 665 nm. The PL band intensity of the samples follow the sequence: Ag_2SeO_4-CP > Ag_2SeO_4-UP > Ag_2SeO_4-MH > Ag_2SeO_4-SC. The lowest PL intensity is mainly associated with a lower recombination rate of electron-hole (e`─h•) pairs. This PL behavior can be attributed to the structural and electronic arrangements of the [$AgO_6$] and [$SeO_4$] clusters. The electronic PL phenomenon occurs after electronic transition from the VB to the CB, forming the e`─h• pairs and subsequently emitting photon decay radiatively. The degree of order-disorder of the constituent clusters is responsible for the presence of vacancies as well as surface and bulk structural defects, which in turn play an important role in the visible emission spectra. Also, different synthesis method can change the lengths and angles of the Ag-O and Se-O bonds, modifying the electronic properties of the materials. The intense orange-red emissions observed in sample Ag_2SeO_4-CP can be ascribed to the deep-level defects located in the optical band gap region. In addition, we assume that CP is the method that provides more induced defects. Then, it can be implied that these crystals present medium-range structural and electronic order-

disorder, resulting in this aforementioned PL behavior characteristic of a multiphonon and multilevel process occurring within the band gap. Similar results were achieved by other silver-based semiconductors, such as Ag_2SeO_3. [44]

Fig. 11(b) illustrates the CIE chromatic diagram and the respective positions of x and y coordinates of the Ag_2SeO_4 crystals obtained through the PL emission spectra. The (x;y) chromatic coordinate positions are located at (0.66; 0.32) for Ag_2SeO_4-SC, (0.68; 0.31) for Ag_2SeO_4-UP, (0.68; 0.32) for Ag_2SeO_4-CP, and (0.67; 0.32) for Ag_2SeO_4-MH. The samples present intense emitting color in the red region, and the (x;y) coordinates are located near the red edge of the diagram. These results confirm the pureness and brightness of the samples as well as their possible use as a new material for optical devices.

Figs. 11(c-f) display the PL emission deconvolution spectra of the Ag_2SeO_4 crystals. The Voigt area G/L function was used for the deconvolution process, resulting in three components centered at 596 nm, 665, and 752 nm. A larger percentage of emission area occurs for the component at 665 nm (around 50%), followed by those at 752 nm (around 25-30%) and at 586 nm (around 20%).

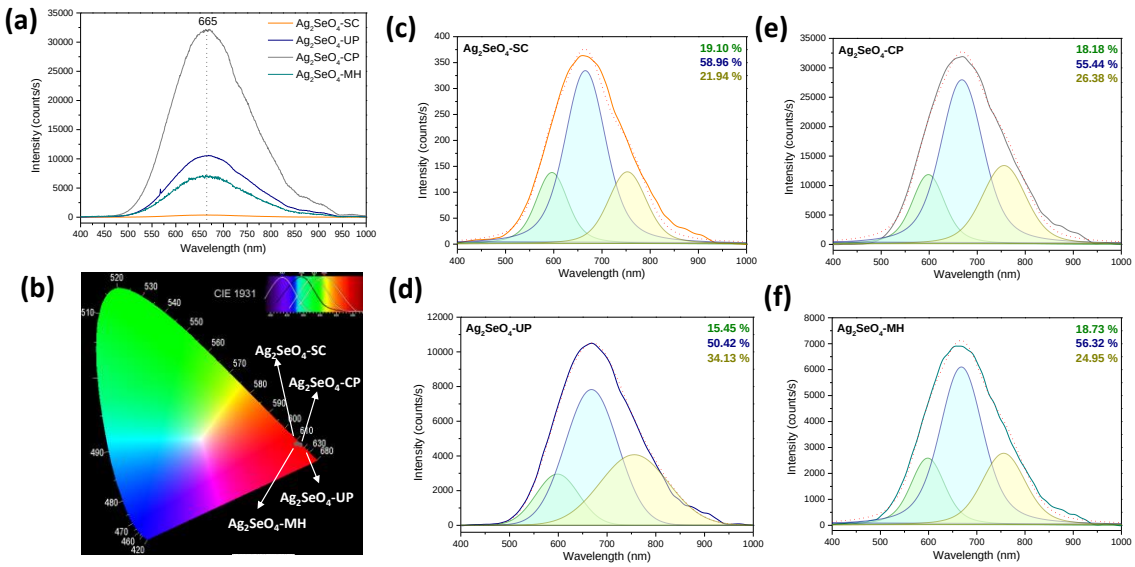

Figure 11. (a) PL emission spectra (λ_{exc} = 355 nm), (b) CIE chromatic diagram and the respective positions of x and y coordinates, and PL deconvolution spectra of (c) Ag_2SeO_4-SC (d), Ag_2SeO_4-UP, (e) Ag_2SeO_4-CP, and (f) Ag_2SeO_4-MH. Inset: percentage of color area for the components.

As previously discussed, the CP method promotes a morphological control of the material with preference exposure of the (111) surface (morphology A in Fig. 9). The chemical environmental of (111) surface is governed by the presence of regular [SeO_4] and defective [$AgO_4 \cdot 2V_O^x$] clusters (Fig. SI-8(e)), with spatial distribution preferential for the Se and Ag cations exposed in the top of the surface, which induce the transference of the excess of electronic density to the interior of the bulk, resulting in a slightly positive surface. An analysis of the electrostatic potential of the (111) surface displayed in Fig. 12(b), confirms this is a positive surface which would increase the PL emission intensity, because a reduced local charge density on the surface decreases the probability of non-radiative transitions, indicating that the recombination rate of the photogenerated electron (e′) and hole (h•) pairs is the largest one.

On the other hand, despite the E_{gap} value for this surface (Fig. SI-8(f)) be very close to the E_{gap} bulk and intermediate levels are not observed in the bulk region, the calculated DOS profile for (111) surface (Fig. SI-8(f)) shown a higher density of states and overlap orbital when compared with the bulk, resulting in distinct photoinduced excitations. Combining these facts, it is expected that shape-oriented Ag_2SeO_4 particles exhibit enhanced PL emissions.

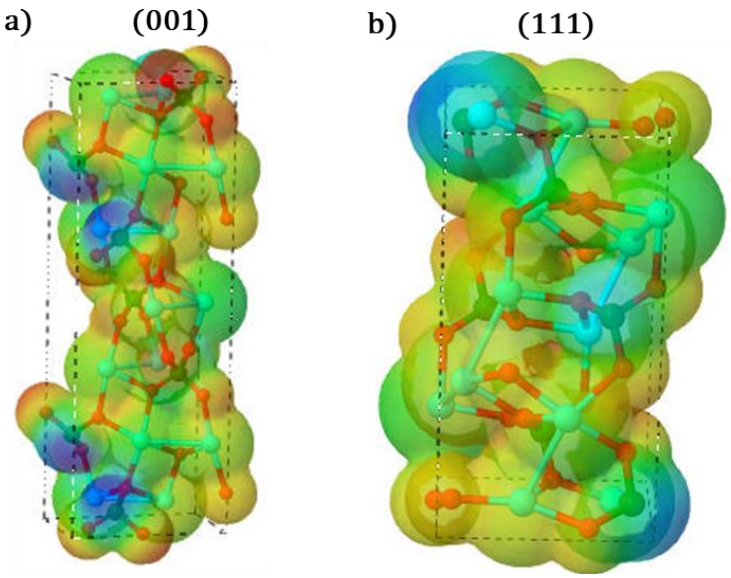

Figure 12. Electrostatic potential maps for (a) (001) surface and (b) (111) surface. The red surface corresponds to a negative region of the electrostatic potential (-0.01 au), whereas the blue color corresponds to the region where the potential is positive (0.010 au).

Photocatalytic activity

The photocatalytic property of the samples was evaluated by spectrophotometry at maximum absorption wavelength (λ_{max} = 554 nm) through the photodegradation of RhB under UV light irradiation. Fig. 13 shows the absorbance spectra of samples Ag_2SeO_4-SC, Ag_2SeO_4-UP, Ag_2SeO_4-CP and Ag_2SeO_4-MH. It can be seen that the Ag_2SeO_4-SC is the sample that most closely matches the absorbance value 0, thus being the sample with the highest photocatalytic activity.

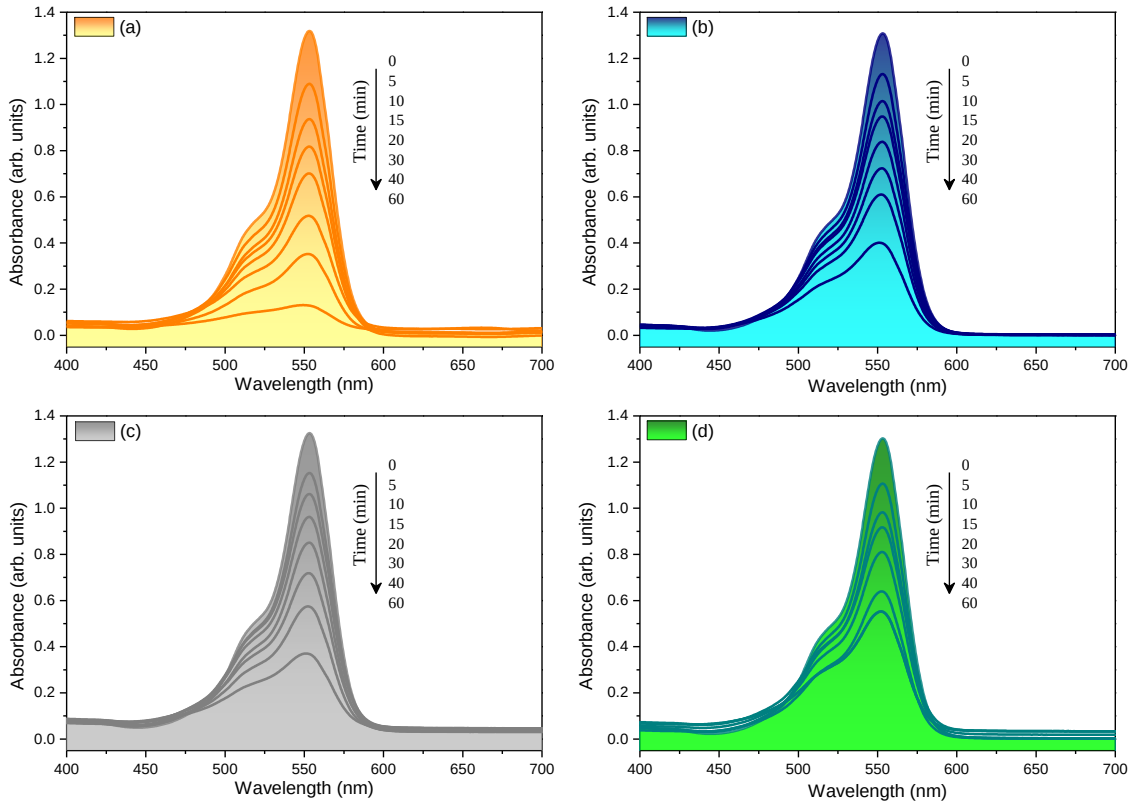

Figure 13. UV-vis absorption spectra of RhB at different time intervals in the presence of Ag_2SeO_4-SC (a), Ag_2SeO_4-UP (b), Ag_2SeO_4-CP (c), and Ag_2SeO_4-MH (d)

The photodegradation efficiency of the sample Ag_2SeO_4-SC can be better observed in Fig. 14(a), which shows the graph of A/A_0 as a function of time (t), where A is the absorbance at certain times and A_0 is the initial absorbance of RhB after the adsorption-desorption process. An experiment without the presence of the catalysts was carried out to demonstrate the efficiency of the synthesized samples (Fig. 14(a)). It can be seen that a greater photodegradation of RhB occurs in the presence of the catalysts,

proving the photocatalytic property of the samples synthesized in this study. Besides, the reaction kinetics of the RhB photodegradation was also calculated in order to investigate the photocatalytic performance, as shown in Fig. 14(b).

The value of the kinetic rate constant can be calculated using the pseudo-first order model ($-\ln(A/A_0) = kt$, where k is the rate constant (min^{-1})). According to Fig. 14(b), the correlation between $-\ln(A/A_0)$ and irradiation time is linear, demonstrating that the photodegradation of the RhB dye follows the first order under UV light illumination. The calculated reaction rate constants k were 0.037, 0.019, 0.020, 0.015, and 0.005 min^{-1} for Ag_2SeO_4-SC, Ag_2SeO_4-UP, Ag_2SeO_4-CP, Ag_2SeO_4-MH, and Ag_2SeO_4 (without catalyst), respectively. The sample synthesized by the sonochemical method showed the highest k value, proving to be the most efficient catalyst for RhB photodegradation. Additionally, the sonochemical approach was also the best method for synthesizing Ag_2SeO_3 catalysts for the photodegradation of RhB under UV light. [44]

It is reported that PL intensity is directly correlated with the recombination of photoexcited e'—h• pairs and that a lower PL intensity means less recombination, leaving the e'—h• pairs free to act on the RhB photodegradation [89]. Sample Ag_2SeO_4-SC showed the lowest PL intensity, as seen in Fig. 11(a), which was also observed by Pinatti et al. [44] for the Ag_2SeO_3 sample synthesized by the sonochemical method. Thus, it is believed that samples synthesized by the sonochemical method tend to have a lower recombination of the e'—h• pair, which is reflected in their higher photocatalytic response. These results present similar behavior as other photocatalyst recently studied [90–95].

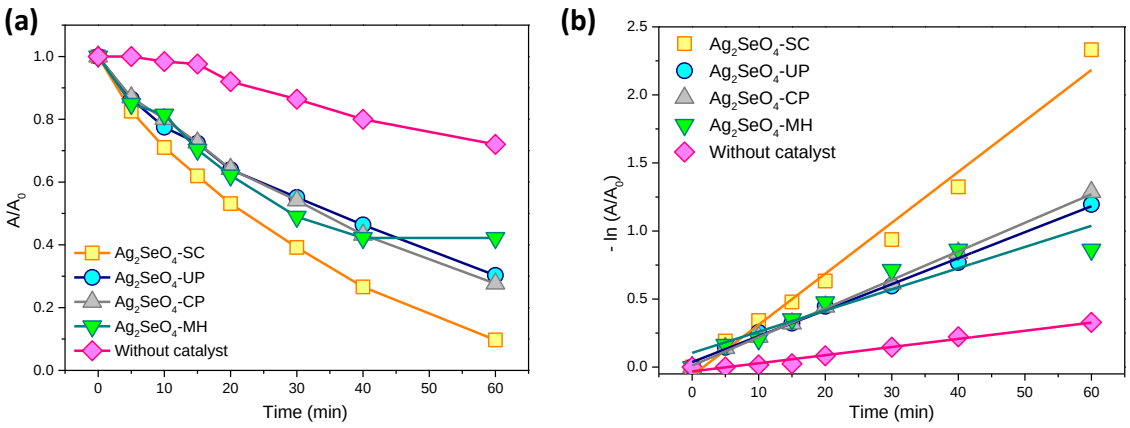

Figure 14. Photocatalytic degradation (a) and kinetic fit curves for all samples under UV-light irradiation (b).

Regarding to the samples obtained by SC method, the rhombus morphologies are formed by (111) and (010) surfaces which are characterized to present regular $[SeO_4]$ and defective $[AgO_4 \cdot 2V_O^x]$ clusters in the top of the surface. In contrast with the (111) surface, the (001) surface display preferentially the O atoms. This spatial orientation of the O atoms along of the surface promote the generation of a negative surface which can be observed in Fig. 12(a), reducing the rate of the recombination of photoexcited e'—h• pairs and promoting the photocatalytic activity.

Photocatalytic mechanism

To understand the photodegradation mechanism of the sample Ag_2SeO_4-SC, which presented the highest photocatalytic activity, experiments were carried out using p-benzoquinone (BQ), ammonium oxalate (AO) and tert-butyl alcohol as scavengers of $O_2^{\cdot}$, h•, and OH*, respectively. According to Fig. 15, the RhB photodegradation efficiency is unaffected by the addition of BQ and TBA, indicating that $O_2^{\cdot}$ and OH* participate, to a lesser extent, in the RhB photodegradation process. When AO is added, the percentage of degradation decreases remarkably, suggesting that h• is largely responsible for the photocatalytic activity of the sample Ag_2SeO_4-SC.

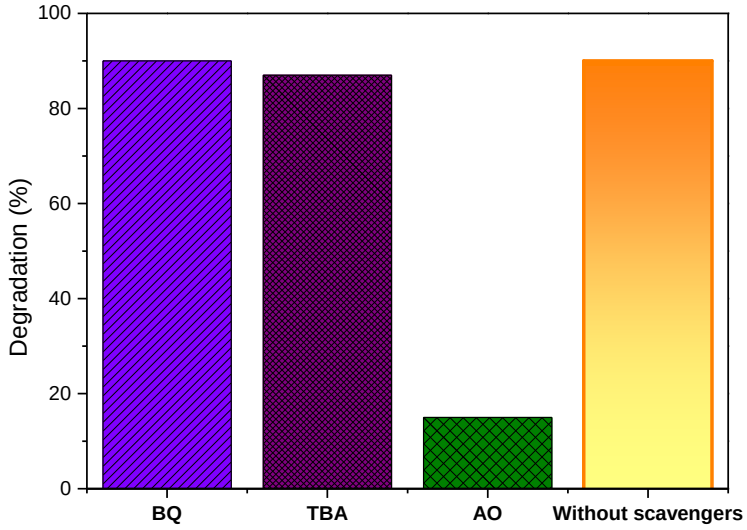

Figure 15. Photocatalytic degradation of RhB using Ag_2SeO_4-SC in the presence of different scavengers under UV-light irradiation

In order to propose the band energy diagram of the sample Ag_2SeO_4-SC, the potential of the conduction band (E_{CB}) and the potential of the valence band (E_{VB}) were calculated using the following equations [96,97]:

$$E_{VB} = \chi - E_e + 0.5E_{gap} \quad \text{Eq. 3}$$

$$E_{CB} = E_{VB} - E_{gap}, \quad \text{Eq. 4}$$

where χ is the absolute electronegativity of the sample Ag_2SeO_4-SC, which was obtained by the geometric mean of the electronegativity of the constituent atoms with a value of 6.25 eV; E_e is the energy of the free electron in hydrogen scale (approximately 4.5 vs NHE); and E_{gap} is the calculated band gap energy. The E_{VB} and E_{CB} values found for this sample were 3.18 and 0.32 eV, respectively. The RhB photodegradation mechanism under UV light irradiation followed the Kröger–Vink notation [88].

As shown in Fig.16, the Ag_2SeO_4-SC is formed by $[AgO_6]^x$ and $[SeO_4]^x$ clusters with neutral charge. When the material is irradiated by UV light, the e' of the $[AgO_6]^x$ cluster are photoexcited to the conduction band (CB), generating in the valence band (VB) of the material clusters with positive charge, such as $[AgO_6]^{\bullet}$, which will act as $h^{\bullet}$. In the CB, the generated clusters have negative charge, such as $[SeO_4]'$, acting as e' (see reaction 1).

$$[AgO_6]^x + [SeO_4]^x + h\nu \rightarrow [AgO_6]^{\bullet} + [SeO_4]' \quad (1)$$

In contrast, $[AgO_6]^{\bullet}$ clusters in the VB, which can act as $h^{\bullet}$, can oxidize RhB directly [98–100] (see reaction 2).

$$[AgO_6]^{\bullet} + RhB \rightarrow \text{degraded products} \quad (2)$$

This is in accordance with the proposed mechanism of photocatalysis, which shows that $h^{\bullet}$ play a crucial role in RhB photodegradation since OH* and $O_2^{\cdot}$ do not participate in the degradation mechanism.

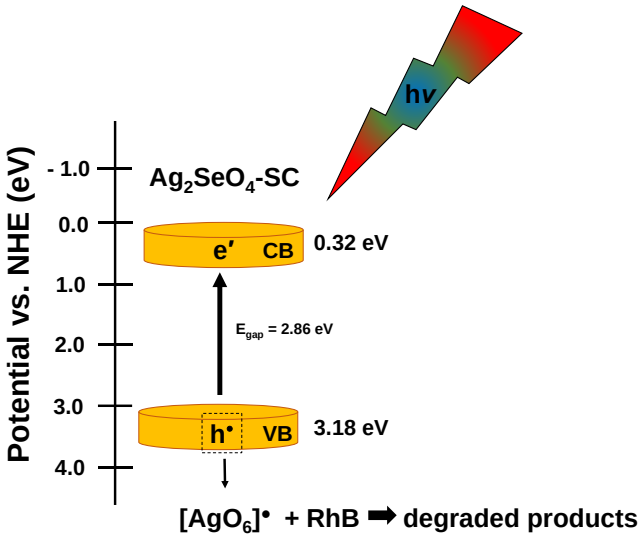

Figure 16. Proposed mechanism for the photodegradation of RhB under UV light irradiation using Ag_2SeO_4-SC

Conclusions

In summary, an orthorhombic Ag_2SeO_4 structure with different morphologies was successfully obtained by four synthesis methods. XRD and Rietveld refinement results confirmed the crystallinity of the samples without secondary phases, while XPS analysis showed that the materials were pure. Raman and FTIR spectroscopies attested the vibrational modes related to Se-O and Ag-O bonds, indicating short-range structural order. FE-SEM images revealed distinct morphologies due to the different methods of synthesis employed. The data obtained by UV-vis DRS spectroscopy and PL emissions were in good agreement with the results of photocatalytic activity. The sample Ag_2SeO_4-SC exhibited the best photocatalyst performance, while the sample Ag_2SeO_4-CP was the one that presented the highest PL emission intensity. Based on the scavenger trapping experiments, the holes and the hydroxyl radical, the former to a lesser extent, were found to be the main reactive species during the photodegradation process, which allowed us to propose a possible photocatalytic mechanism. The relative stability of the Ag_2SeO_4 surfaces was calculated using the Wulff construction in order to rationalize the crystal morphologies observed in the FE-SEM images and determine different energy profiles associated with the transformation processes among morphologies. Lastly, the results presented herein confirm that Ag_2SeO_4 is a promising photocatalyst with enhanced optical properties.

Conflicts of interest

There are no conflicts to declare.

Acknowledgments

The authors are grateful to the São Paulo Research Foundation (FAPESP) (grant Nos. 13/07296-2, 18/09530-6, 19/03722-3, and 19/25944-8), and the Coordination for the Improvement of Higher Education Personnel (CAPES) for the financial support. They also wish to thank Prof. Valmor Roberto Mastelaro (IFSC-USP), Rorivaldo Camargo (CDMF-UFSCar), and Sandra Maria Terenzi Bellini (CDMF-UFSCar) for the technical and scientific contributions. J.A. is grateful to the Universitat Jaume I (Project UJI-B2019-30) and the Ministerio de Ciencia, Innovación y Universidades (Spain) (Project PGC2018-094417-B-I00) for supporting this research financially. The electronic potential maps calculations were performed at the Center of Mathematical Sciences Applied to Industry (CeMEAI) funded by FAPESP (grant No. 2013/07375-0).

Electronic Supporting Information

The electronic supplementary information contains: Rietveld refinement plot, atomic positions, crystallographic data of Rietveld refinement, XPS core level spectra and XPS elements positions and concentration of the area components, band gap energy, crystal shapes theoretically modeled by the Wulff construction and theoretical parameters of the surfaces.

References

1 M. Qie, J. Lin, F. Kong, M. A. Silver, Z. Yue, X. Wang, L. Zhang, H. Bao, T. E. Albrecht-Schmitt and J. Q. Wang, *Inorganic Chemistry*, 2018, **57**, 1676–1683.

2 S. V. Krivovichev, V. Kahlenberg, R. Kaindl, E. Mersdorf, I. G. Tananaev and B. F. Myasoedov, *Angewandte Chemie*, 2005, **117**, 1158–1160.

3 J. Ling, G. E. Sigmon and P. C. Burns, *Journal of Solid State Chemistry*, 2009, **182**, 402–408.

4 C. N. R. Rao, J. N. Behera and M. Dan, *Chemical Society Reviews*, 2006, **35**, 375–387.

5 M. Shang and P. S. Halasyamani, *Journal of Solid State Chemistry*, 2020, **286**, 2–7.

6 D. Yi, S. Sanghvi, C. P. Kowalski and S. M. Haile, *Chemistry of Materials*, 2019, **31**, 9807–9818.

7 H. Matsui, K. Shimatani, Y. Ikemoto, T. Sasaki and Y. Matsuo, *Journal of Chemical Physics*, , DOI:10.1063/1.5145108.

8 G. Giester and M. Wildner, *Journal of Solid State Chemistry*, 1991, **91**, 370–374.

9 O. Rademacher, H. Göbel and H. Oppermann, *Zeitschrift fur Kristallographie - New Crystal Structures*, 2000, **215**, 339–340.

10 L. Shi, D. Mei, J. Xu and Y. Wu, *Solid State Sciences*, 2016, **63**, 54–61.

11 Y. X. Ma, Y. P. Gong, C. L. Hu, F. Kong and J. G. Mao, *Inorganic Chemistry*, 2020, **59**, 7852–7859.

12 and K. M. O. Jee Yoon Chung, Hongil Jo, Seongbeom Yeon, Hye Ryung Byun, Tae-Soo You, Joon I. Jang, *Chemistry of Materials*, 2020, **32**, 7318–7326.

13 D. W. Lee, S. J. Oh, P. S. Halasyamani and K. M. Ok, *Inorganic Chemistry*, 2011, **50**, 4473–4480.

14 G. G. Gospodinov and M. G. Stancheva, *Journal of Chemical Information and Modeling*, 2019, **53**, 1689–1699.

15 S. E. Bang, D. W. Lee and K. M. Ok, *Inorganic Chemistry*, 2014, **53**, 4756–4762.

16 A. J. Tuxworth, C. H. Wang and J. S. O. Evans, *Dalton Transactions*, 2015, **44**, 3009–3019.

17 J. Gu, Z. Q. Zhao, Y. Ding, H. L. Chen, Y. W. Zhang and C. H. Yan, *J Am Chem Soc*, 2013, **135**, 8363–8371.

18 M. Ionashiro, C. B. Melios, C. A. Ribeiro, M. S. Crepsi and I. Giolito, *Thermochimica Acta*, 1990, 168, 223–232.

19 M. de Pedro, J. C. Trombe and A. Castro, *Journal of Materials Science Letters*, 1995, **14**, 994–997.

20 G. Steinhauser, C. Luef, M. Wildner and G. Giester, *Journal of Alloys and Compounds*, 2006, **419**, 45–49.

21 M. Wildner and G. Giester, *Neues Jahrbuch fur Mineralogie, Abhandlungen*, 2007, **184**, 29–37.

22 W. Bensch and J. R. Gunter, 1986, **174**, 291–295.

23 K. Kohn, K. Inoue, O. Horie and S. I. Akimoto, *Journal of Solid State Chemistry*, 1976, **18**, 27–37.

24 M. E. Essington, *Soil Science Society of America Journal*, 1988, **52**, 1574–1579.

25 H. Pristacz, D. Talla, F. Preuschl, G. Giester and M. Wildner, *N. JB. Miner. Abh. (J. Min. Geochem.)*, 2014, **191**, 215–223.

26 C. W. F. T. Pistorius and M. C. Pistorius, *Zeitschrift fur Kristallographie. Bd.*, 1962, **117**, 259–271.

27 M. F. C. Ladd and W. H. Lee, *Journal of Inorganic and Nuclear Chemistry*, 1961, **21**, 216–220.

28 I. Karakaya and W. T. Thompson, *Bulletin of Alloy Phase Diagrams*, 1990, **11**, 266–271.

29 C. W. F. T. Pistorius and J. E. Kräger, *ZAAC - Journal of Inorganic and General Chemistry*, 1967, **352**, 222–224.

30 C. W. F. T. Pistorius, *The Journal of Chemical Physics*, 1967, **46**, 2167–2171.

31 C. W. F. T. Pistorius and J. C. A. Boeyens, *Zeitschrift fur Anorganische und Allgemeine Chemie*, 1970, **222**, 263–267.

32 F. Bonino, C. Forte, M. Lazzari and B. Scrosati, *Journal of Power Sources*, 1978, **3**, 257–265.

33 Z. Boncheva-Mladenova and N. Dishovsky, *Journal of Crystal Growth*, 1979, **47**, 467–468.

34 N. Dishovsky and Z. Boncheva-Mladenova, *Journal of Crystal Growth*, 1981, **51**, 147–148.

35 T. Minami, K. Imazawa and M. Tanaka, *Journal of Non-Crystalline Solids*, 1980, **42**, 469–476.

36 M. C. R. Shastry and K. J. Rao, *Proc. Indian Acad. Sci.*, 1990, **102**, 541–553.

37 C. Cramer, D. L. Price and M. L. Saboungi, *Journal of Physics Condensed Matter*, 1998, **10**, 6229–6242.

38 C. Cramer and M. Buscher, *Solid State Ionics*, 1998, **105**, 109–120.

39 C. Cramer, M. Grimsditch and M.-L. Saboungi, *The Journal of Physical Chemistry B*, 1999, **103**, 4018–4022.

40 L. Pejov and V. M. Petruševski, *Journal of Physics and Chemistry of Solids*, 2001, **62**, 521–530.

41 M. Weil, *Z. Natusforsch*, 2003, **58b**, 1091–1096.

42 D. Pitzschke, J. Curda, G. Cakmak and M. Jansen, *Zeitschrift fur Anorganische und Allgemeine Chemie*, 2008, **634**, 1071–1076.

43 I. Minenkova, V. V. Sliznev, L. Cavallo and Y. Minenkov, *Inorganic Chemistry*, 2019, **58**, 7873–7885.

44 I. M. Pinatti, A. B. Trench, A. C. M. Tello, P. F. S. Pereira, J. C. Souza, M. D. Teodoro, I. L. V Rosa, J. Andres, E. Longo and A. Z. Simo, *Inorganic Chemistry*, 2021, **60**, 5937–5954.

45 R. Dovesi, A. Erba, R. Orlando, C. M. Zicovich-Wilson, B. Civalleri, L. Maschio, M. Rérat, S. Casassa, J. Baima, S. Salustro and B. Kirtman, *Wiley Interdisciplinary Reviews: Computational Molecular Science*, 2018, **8**, 1–36.

46 D. Andrae, U. Häußermann, M. Dolg, H. Stoll and H. Preuß, *Theoretica Chimica Acta*, 1990, **77**, 123–141.

47 M. F. Peintinger, D. V. Oliveira and T. Bredow, *Journal of Computational Chemistry*, 2013, **34**, 451–459.

48 A. D. Becke, *The Journal of Chemical Physics*, 1993, **98**, 5648–5652.

49 P. J. Stephen, F. J. Devlin, C. F. Chabalowski and M. J. Frisch, *The Journal of Physical Chemistry*, 1994, **98**, 11623–11627.

50 B. G. Pfrommer, M. Côté, S. G. Louie and M. L. Cohen, *Journal of Computational Physics*, 1997, **131**, 233–240.

51 G. D. Barmparis, Z. Lodziana, N. Lopez and I. N. Remediakis, *Beilstein Journal of Nanotechnology*, 2015, **6**, 361–368.

52 J. Andrés, L. Gracia, A. F. Gouveia, M. M. Ferrer and E. Longo, *Nanotechnology*, 2015, **26**, 405703.

53 M. M. Ferrer, A. F. Gouveia, L. Gracia, E. Longo and J. Andrés, *Modelling and Simulation in Materials Science and Engineering*, 2016, **24**, 025007.

54 N. G. Macedo, A. F. Gouveia, R. A. Roca, M. Assis, L. Gracia, J. Andrés, E. R. Leite and E. Longo, *Journal of Physical Chemistry C*, 2018, **122**, 8667–8679.

55 J. R. Reimers, Z. L. Cai, A. Bilić and N. S. Hush, *Ann N Y Acad Sci*, 2003, **1006**, 235–251.

56 B. H. Toby, *J. Appl. Crystallogr.*, 2001, **34**, 210–213.

57 L. W. Finger, D. E. Cox and A. P. Jephcoat, *Journal of Applied Crystallography*, 1994, **27**, 892–900.

58 P. W. Stephens, *Journal of Applied Crystallography*, 1999, **32**, 281–289.

59 K. Momma and F. Izumi, *Journal of Applied Crystallography*, 2011, **44**, 1272–1276.

60 K. Momma and F. Izumi, *Journal of Applied Crystallography*, 2008, **41**, 653–658.

61 J. Zhu, H. Fan, J. Sun and S. Ai, *Separation and Purification Technology*, 2013, **120**, 134–140.

62 Z. Lin, J. Li, Z. Zheng, J. Yan, P. Liu, C. Wang and G. Yang, *ACS Nano*, 2015, **9**, 7256–7265.

63 Z. Wang, Q. Sun, D. Wang, Z. Hong, Z. Qu and X. Li, *Separation and Purification Technology*, 2019, **209**, 1016–1026.

64 M. Zhou, Z. Wang, Q. Sun, J. Wang, C. Zhang, D. Chen and X. Li, *ACS Applied Materials and Interfaces*, 2019, **11**, 46875–46885.

65 X. Zhang, Y. Yang, L. Song, Y. Wang, C. He, Z. Wang and L. Cui, *Molecular Catalysis*, 2018, **447**, 80–89.

66 S. Mangavati, A. Pal, A. Rao, Z. Z. Jiang and Y. K. Kuo, *Journal of Physics and Chemistry of Solids*, 2022, **160**, 110301.

67 M. Gui, J. K. Papp, A. S. Colburn, N. D. Meeks, B. Weaver, I. Wilf and D. Bhattacharyya, *Journal of Membrane Science*, 2015, **488**, 79–91.

68 J. R. Shallenberger, *Surface Science Spectra*, 2018, **25**, 014001.

69 H. Cai, L. Yao, Y. Xia, C. Dao, J. Li, L. Lin, Z. Huang and G. Chen, *Solar Energy*, 2019, **193**, 986–991.

70 Y. Tong, T. Jiang, A. Bendounan, F. Nicolas, S. Kubsky and V. A. Esaulov, *Journal of Physical Chemistry C*, 2016, **120**, 21486–21495.

71 Y. Huang, Y. E. Miao, J. Fu, S. Mo, C. Wei and T. Liu, *Journal of Materials Chemistry A*, 2015, **3**, 16263–16271.

72 X. Cui, S. H. Yu, L. Li, L. Biao, H. Li, M. Mo and X. M. Liu, *Chemistry - A European Journal*, 2004, **10**, 218–223.

73 S. Huang, X. Zhang, L. Wang, L. Bai, J. Xu, C. Li and P. Yang, *Dalton Transactions*, 2012, **41**, 5634–5642.

74 J. Andrés, L. Gracia, P. Gonzalez-Navarrete, V. M. Longo, W. Avansi, D. P. Volanti, M. M. Ferrer, P. S. Lemos, F. A. La Porta, A. C. Hernandes and E. Longo, *Scientific Reports*, 2014, **4**, 1–7.

75 X. Y. Zhang, J. D. Wang, J. K. Liu, X. H. Yang and Y. Lu, *CrystEngComm*, 2015, **17**, 1129–1138.

76 X. Tan, Q. Fan, X. Wang and B. Grambow, *Environmental Science and Technology*, 2009, **43**, 3115–3121.

77 B. Y. Wang, G. Y. Zhang, G. W. Cui, Y. Y. Xu, Y. Liu and C. Y. Xing, *Inorganic Chemistry Frontiers*, 2019, **6**, 209–219.

78 A. C. Catto, T. Fiorido, É. L. S. Souza, W. Avansi, J. Andres, K. Aguir, E. Longo, L. S. Cavalcante and L. F. da Silva, *Journal of Alloys and Compounds*, 2018, **748**, 411–417.

79 P. Okkonen, L. Hiltunen, M. Koskenlinna and L. Niinisto, *Acta Chemica Scandinavica*, 1994, **48**, 857–860.

80 A. Bachvarova, Y. Dimitriev and R. Iordanova, *Journal of Non-Crystalline Solids*, 2005, **351**, 998–1002.

81 K. Sathianandan, L. D. McCory and J. L. Margrave, *Spectrochimica Acta*, 1964, **20**, 957–963.

82 A. J. Kora and L. Rastogi, *Journal of Environmental Management*, 2016, **181**, 231–236.

83 J. Ma, Y. Wang, L. Zhou and S. Zhang, *Materials Science and Engineering C*, 2013, **33**, 440–445.

84 B. Deb and A. Ghosh, *Journal of Nanoscience and Nanotechnology*, 2010, **10**, 6752–6759.

85 D. L. Wood and J. Tauc, *Physical Review B*, 1972, **5**, 3144–3151.

86 X. Jin, I. Y. Kim, Y. K. Jo, J. L. Bettis, H. J. Koo, M. H. Whangbo and S. J. Hwang, *Journal of Physical Chemistry C*, 2013, **117**, 26509–26516.

87 L. X. Lovisa, M. C. Oliveira, J. Andrés, L. Gracia, M. S. Li, E. Longo, R. L. Tranquilin, C. A. Paskocimas, M. R. D. Bomio and F. V. Motta, *Journal of Alloys and Compounds*, 2018, **750**, 55–70.

88 F. A. Kröger and H. J. Vink, *Solid State Physics - Advances in Research and Applications*, 1956, **3**, 307–435.

89 R. Wu, H. Song, N. Luo and G. Ji, *Journal of Colloid and Interface Science*, 2018, **524**, 350–359.

90 G. Duoerkun, Y. Zhang, Z. Shi, X. Shen, W. Cao, T. Liu, J. Liu, Q. Chen and L. Zhang, *Advanced Fiber Materials*, 2020, **2**, 13–23.

91 Y. Sun, J. B. Mwandeje, L. M. Wangatia, F. Zabihi, J. Nedeljković and S. Yang, *Advanced Fiber Materials*, 2020, **2**, 118–122.

92 C. Wang, M. Cai, Y. Liu, F. Yang, H. Zhang, J. Liu and S. Li, *Journal of Colloid and Interface Science*, 2022, **605**, 727–740.

93 S. Yang, D. K. Macharia, S. Ahmed, B. Zhu, Q. Zhong, H. Wang and Z. Chen, *Advanced Fiber Materials*, 2020, **2**, 150–160.

94 S. Xiong, Y. Yu, P. Wang, M. Liu, S. Chen, X. Yin, L. Wang and H. Wang, *Advanced Fiber Materials*, 2020, **2**, 246–255.

95 S. Li, X. Shen, J. Liu and L. Zhang, *Environmental Science: Nano*, 2017, **4**, 1155–1167.

96 M. A. Butler and D. S. Ginley, *Journal of The Electrochemical Society*, 1978, **125**, 228–232.

97 Z. Ma, Z. Yi, J. Sun and K. Wu, *Journal of Physical Chemistry C*, 2012, **116**, 25074–25080.

98 M. Danish and M. Muneer, *Ceramics International*, 2021, **47**, 13043–13056.

99 Z. Tong, D. Yang, T. Xiao, Y. Tian and Z. Jiang, *Chemical Engineering Journal*, 2015, **260**, 117–125.

100 Y. Sang, X. Cao, G. Dai, L. Wang, Y. Peng and B. Geng, *Journal of Hazardous Materials*, 2020, **381**, 120942.